

Anomalous quantum scattering and transport of electrons with Mexican-hat band structure induced by electrical potential

Jia-Ting Yao(姚嘉婷), Ben-Liang Zhou(周本良), Xiao-Ying Zhou(周小英), Xian-Bo Xiao(肖贤波), and Guang-Hui Zhou(周光辉)

Citation: Chin. Phys. B, 2026, 35 (**3**): 037203. DOI: 10.1088/1674-1056/adecfb
http://cpb.iphy.ac.cn; http://iopscience.iop.org/cpb

What follows is a list of articles you may be interested in

Current-perpendicular-to-plane transport properties of 2D ferromagnetic material $CrTe_2$

Jin Wang(王瑾), Yu Liu(刘宇), Taikun Wang(王太坤), Yongkang Xu(徐永康), Shuanghai Wang(王双海), Kun He(何坤), Yafeng Deng(邓亚峰), Pengfei Yan(闫鹏飞), and Liang He(何亮)

Chin. Phys. B, 2024, 33 (**9**): 097201. DOI: 10.1088/1674-1056/ad5af1

Valley-dependent transport in a mescoscopic twisted bilayer graphene device

Wen-Xuan Shi(史文萱), Han-Lin Liu(刘翰林), and Jun Wang(汪军)

Chin. Phys. B, 2024, 33 (**1**): 017205. DOI: 10.1088/1674-1056/acf9e4

Tunable caging of excitation in decorated Lieb-ladder geometry with long-range connectivity

Atanu Nandy

Chin. Phys. B, 2023, 32 (**12**): 127201. DOI: 10.1088/1674-1056/acf5ce

Electron tunneling through double-electric barriers on HgTe/CdTe heterostructure interface

Liang-Zhong Lin(林亮中), Yi-Yun Ling(凌艺纭), Dong Zhang(张东), and Zhen-Hua Wu(吴振华)

Chin. Phys. B, 2022, 31 (**11**): 117201. DOI: 10.1088/1674-1056/ac7a0f

Spin transport in a chain of polygonal quantum rings with Dresselhaus spin-orbit coupling

Han-Zhao Tang(唐翰昭), Xiao-Teng Yao(要晓腾), Jian-Jun Liu(刘建军)

Chin. Phys. B, 2017, 26 (**11**): 117203. DOI: 10.1088/1674-1056/26/11/117203

Anomalous quantum scattering and transport of electrons with Mexican-hat band structure induced by electrical potential

Jia-Ting Yao(姚嘉婷)[1], Ben-Liang Zhou(周本良)[1], Xiao-Ying Zhou(周小英)[2,1,†], Xian-Bo Xiao(肖贤波)[3,‡], and Guang-Hui Zhou(周光辉)[4]

[1] *Department of Physics, Key Laboratory for Low-Dimensional Structures and Quantum Manipulation (Ministry of Education), Hunan Normal University, Changsha* 410081, *China*

[2] *School of Physics and Electronics, Hunan Provincial Key Laboratory of Intelligent Sensors and Advanced Sensor Materials, Hunan University of Science and Technology, Xiangtan* 411201, *China*

[3] *School of Computer Science, Jiangxi University of Chinese Medicine, Nanchang* 330004, *China*

[4] *Department of Physics, Shaoyang University, Shaoyang* 422001, *China*

(Received 7 May 2025; revised manuscript received 21 June 2025; accepted manuscript online 8 July 2025)

We theoretically study the quantum scattering and transport of electrons with Mexican-hat dispersion through both step and rectangular potential barriers by using the transfer matrix method. Owing to the torus-like iso-energy lines of the Mexican-hat dispersion, abnormal retro-reflection (RR) and specular transmission (ST) are generated besides the normal reflection (NR) and transmission (NT). For the step potential with electrons incident from the large wavevector, the transmission is primarily governed by NT with nearly negligible ST, while the reflection is dominant by RR (NR) within (outside) the critical angle. Additionally, for electrons incident from the small wavevector, the NT can be reduced to zero by adjusting the barrier, resulting in a significant enhancement of ST and RR. For the rectangular barrier, the transmission and reflection spectra resemble those of the step barrier, but there are two kinds of resonant tunneling which can lead to perfect NT or ST. Due to the anomalous scattering process, the conductance of the system can be effectively controlled by adjusting the height and width of the barrier as well as the incident energy. Our results provide a deeper understanding of the electron states governed by the Mexican-hat dispersion.

Keywords: quantum scattering and transport, transfer matrix method, Mexican-hat dispersion

PACS: 72.10.–d, 72.20.Dp, 73.23.–b

DOI: 10.1088/1674-1056/adecfb **CSTR:** 32038.14.CPB.adecfb

1. Introduction

The discovery of graphene in 2004 marked the beginning of extensive research on two-dimensional (2D) materials.[1] Since then, 2D materials have rapidly gained prominence in condensed matter physics due to their critical dimensions, atomic thickness, and diverse band structures.[2–4] Many excellent and exotic properties associated to 2D materials can not be found in their bulk counterparts.[2–7] To date, a considerable number of new 2D materials have been both theoretically predicted and experimentally synthesized.[5–7] The band structures of 2D materials change qualitatively as the thickness is reduced to few or monolayer. The most famous example is graphene, which has a linear dispersion near the Fermi level, requiring a description by 2D Dirac equation.[8] Indirect–direct band gap transition occurs when the thickness of 2D transition metal dichalcogenides (TMDCs) decreases to monolayer.[9] For some 2D materials, the band structure undergos a transformation from a parabolic dispersion into a Mexican-hat shape as their thickness decreases to monolayer, which is also known as a Lifshiftz transition.[10] Several 2D electron systems possess Mexican-hat dispersion in the low energy regime, as confirmed by experiments.[11–18] Notable examples include the gated bilayer graphene,[11] the inverted InAs/GaSb double quantum well,[12] and the ultrathin 2D group IIIA metal chalcogenides MX (M = Ga, In and X = S, Se, Te).[13–18] Interestingly, the Mexican-hat shaped bands can be tuned by strain or electric fields. For instance, in monolayer InSe, the brim of the Mexican-hat bands can be continuously manipulated by strain[19,20] or a vertical electric field,[21–23] accompanying with an indirect–direct band gap transition.

A prominent feature of Mexican-hat-shaped bands is the singularity in the density of states at or near the band edge, where the density of modes exhibits an abrupt step function.[24–32] The distorted density of states results in exotic electric and magnetic properties in electron systems with sombrero-shaped dispersion,[24–32] such as the multi-ferroic effect in α-SnO,[25] tunable magnetism and half-metallicity monolayer GaSe,[27] the enhanced thermoelectric efficiency in few-layer III–VI materials,[28–31] and the Lifshitz transitions in 2D InSe.[32] In addition, the interplay between the Mexican-hat dispersion and the Rashba/Dresselhaus spin–orbit cou-

†Corresponding author. E-mail: xyzhou@hnust.edu.cn

‡Corresponding author. E-mail: 20101034@jxutcm.edu.cn

© 2026 Chinese Physical Society and IOP Publishing Ltd. All rights, including for text and data mining, AI training, and similar technologies, are reserved.

pling may result in the spin-charge conversion,[33] spin polarization,[34] and a novel 2D Fabry–Pérot oscillation.[35] In conventional semiconductors, the Fermi surface is a circle, and electron scattering against potential barrier follows a Snell's law akin to optics,[36] resulting in specular reflection and normal transmission. This behavior is also observed in graphene. However, graphene p–n junctions exhibit exotic negative refraction,[37,38] which is useful to focus the electron beam. For electrons with Mexican-hat shaped bands, the Fermi surfaces are two concentric circles, similar to a torus. There are two extra scattering channels, which will give rise to novel scattering features when electrons encounter a potential barrier. However, this topic remains unexplored, and the underlying scattering mechanisms are exclusive.

In this paper, we theoretically study the quantum scattering and transport of electrons with Mexican-hat dispersion through both step and rectangular potential barriers by using the transfer matrix method. It is found that the characteristics of the reflections and transmissions are dependent of the injected electron with the large or small wavevector. Moreover, resonant tunneling are observed in the rectangle barrier case, which can lead to perfect transmissions. Owing to the singular quantum scattering process, the conductance of these systems can be effectively controlled by adjusting the height and width of the barrier as well as the incident energy.

The rest of this paper is organized as follows. In Section 2, the quartic model and transfer matrix method for the Mexican-hat-dispersion electrons are introduced. In Section 3, numerical results and discussions for the scattering and transport of Mexican-hat-dispersion electrons are presented. Finally, a brief summary of the results is given in Section 4.

2. Model and methods

The simplest Mexican-hat dispersion takes the form of the quartic model[39]

$$E(k) = h_1 k^2 + h_2 k^4 - E_{\mathrm{T}}, \tag{1}$$

where h_1 and h_2 are constants meeting the conditions $h_1 < 0$ and $h_2 > 0$ for the conduction band while $h_1 > 0$ and $h_2 < 0$ for the valence band. The energy $E_{\mathrm{T}} = -h_1^2/4h_2$ represents the height of the Mexican hat, and $\boldsymbol{k} = (k_x, k_y)$ is the wave vector. For a fixed electron energy E, we have $k^2 = \left(-h_1 \pm \sqrt{h_1^2 + 4h_2(E+E_{\mathrm{T}})}\right)/2h_2$, which means the iso-energy lines, i.e., the Fermi surfaces, are two concentric circles. Their radii are $k_\pm = \left[(-h_1 \pm \gamma)/2h_2\right]^{1/2}$ with $\gamma = \sqrt{h_1^2 + 4h_2(E+E_{\mathrm{T}})}$, where k_+ (k_-) indicates the small (big) iso-energy circles. The probability current density along the two direction can be obtained by $\boldsymbol{j} = -(\mathrm{i}/\hbar)[\boldsymbol{r}, H]$, which are given by $j_{x/y} = k_{x/y}\left(h_1 + 2h_2 k^2\right) = \pm\gamma k_{x/y}$. Therefore, the direction of the probability current density $\boldsymbol{j}$ is identical (opposite) to the direction of the wave vector $\boldsymbol{k}$ on the small (big) iso-energy circle.

Firstly, we consider the scattering at interface of a step potential barrier along the x-direction with the height V as shown in Fig. 1(a). According to the Mexican-hat dispersion shown in Fig. 1(c), we can divide the incident electron energy E into two distinct regimes, each giving rise to different scattering mechanisms. The first regime is $-E_{\mathrm{T}} < E < 0$, as indicated by the light cyan region in Fig. 1(c), in which the electron energy is confined within the Mexican-hat. In this scenario, at a specific energy level, there exist four modes as shown in Fig. 1(c), two propagating forward ($-k_1$ and k_2 states) and two propagating backward ($-k_2$ and k_1 states). Consequently, one will observe retro-reflection and specular transmission, i.e., the negative refraction, in addition to the normal reflection and transmission, which is absent in the electron scattering of conventional 2D electron gas. Since there are two modes propagating forward along the x -direction, we should discuss them separately. If the electron is incident with the wave vector $-k_1$, the wave functions in the incident/reflection ($x < 0$) and the transmission ($x > 0$) regions in Fig. 1(a) can be expressed respectively as

$$\begin{aligned} \psi_1(x) &= \mathrm{e}^{-\mathrm{i}k_{x1}x} + r_1\,\mathrm{e}^{\mathrm{i}k_{x1}x} + r_2\,\mathrm{e}^{-\mathrm{i}k_{x2}x}, \\ \psi_2(x) &= t_1\,\mathrm{e}^{\mathrm{i}k_{x3}x} + t_2\,\mathrm{e}^{-\mathrm{i}k_{x4}x}, \end{aligned} \tag{2}$$

where $k_{xi} = (k_i^2 - k_y^2)^{1/2}$, $i = 1,2,3,4$. The wavevectors k_i are $k_1 = k_+$, $k_2 = k_-$, $k_3 = \left[(-h_1 + \chi)/2h_2\right]^{1/2}$, and $k_4 = \left[(-h_1 - \chi)/2h_2\right]^{1/2}$ with $\chi = \left[h_1^2 + 4h_2(E_{\mathrm{T}} + E - V)\right]^{1/2}$. We have omitted the common factor $\mathrm{e}^{\mathrm{i}k_y y}$ in Eq. (2) because the wavevector k_y is conserved arising from the translation invariance along the y-direction.

The type of each scattering (r_i and t_i, $i = 1,2$) can be classified according to the relative orientation between the wave vector and the group velocity of both reflected and transmitted electrons. The group velocity for a given k states is $\boldsymbol{v}_{\mathrm{g}}(k) = (1/\hbar)\nabla_k E_h(k)$. We can use the product of the wave vector and the group velocity to manifest the relative orientation between them. For the reflected electron state with wave vector k_{x1}, we have $k_{x1} \cdot \boldsymbol{v}_{\mathrm{g}}(k_1) < 0$, which is consistent with that of the incident electron state. Therefore, this is a normal reflection (NR) with magnitude r_1 , as indicated in Fig. 1(a). However, for another reflected electron state wave vector $-k_{x2}$, we have $-k_{x2} \cdot \boldsymbol{v}_{\mathrm{g}}(-k_2) > 0$, which is opposite to that of the incident electron state so that it is a retro-reflection (RR) with magnitude r_2. Similarly, for the transmitted electron states k_3 and $-k_4$, we have $k_{x3} \cdot \boldsymbol{v}_{\mathrm{g}}(k_3) > 0$ and $-k_{x4} \cdot \boldsymbol{v}_{\mathrm{g}}(-k_4) < 0$, which corresponding to the specular transmission (ST) and normal transmission (NT) with magnitude t_1 and t_2, respectively.

Since the Hamiltonian in Eq. (1) contains the quartic term of k, the wave functions in both regions and their first to third

order derivatives should be continuous at the scattering interface $x=0$,[40] i.e., $\psi_1(0)=\psi_2(0), \psi_1'(0)=\psi_2'(0), \psi_1''(0)=\psi_2''(0), \psi_1'''(0)=\psi_2'''(0)$. Once these boundary conditions are considered, we obtain the reflection and transmission coefficients as follows:

$$r_1=\frac{(k_{x1}-k_{x2})(k_{x1}-k_{x4})(k_{x1}+k_{x3})}{(k_{x1}-k_{x3})(k_{x1}+k_{x2})(k_{x1}+k_{x4})}, \tag{3}$$

$$r_2=-2k_{x1}\frac{(k_{x1}-k_{x4})(k_{x1}+k_{x3})}{(k_{x2}-k_{x4})(k_{x1}+k_{x2})(k_{x2}+k_{x3})}, \tag{4}$$

$$t_1=2k_{x1}\frac{(k_{x1}-k_{x2})(k_{x1}-k_{x4})}{(k_{x1}-k_{x3})(k_{x2}+k_{x3})(k_{x3}+k_{x4})}, \tag{5}$$

$$t_2=-2k_{x1}\frac{(k_{x1}-k_{x2})(k_{x1}+k_{x3})}{(k_{x2}-k_{x4})(k_{x1}+k_{x4})(k_{x3}+k_{x4})}. \tag{6}$$

Further, the probability current density operator j in the Mexican hat dispersion can be derived by $j=-(\mathrm{i}/\hbar)[r,H]$ so that the x-component of the probability current density is given as $j_x=k_x\left[h_1+2h_2\left(k_x^2+k_y^2\right)\right]$. According to the conservation of the probability current, the reflection probabilities of the NR and RR are obtained as

$$R_1=|r_1|^2,\quad R_2=\mathrm{Re}\left[\frac{k_{x2}}{k_{x1}}\right]|r_2|^2\left|\frac{h_1+2h_2\left(k_{x2}^2+k_y^2\right)}{h_1+2h_2\left(k_{x1}^2+k_y^2\right)}\right|. \tag{7}$$

The transmission probabilities of the ST and NT are

$$\begin{aligned}T_1&=\mathrm{Re}\left[\frac{k_{x3}}{k_{x1}}\right]|t_1|^2\left|\frac{h_1+2h_2\left(k_{x3}^2+k_y^2\right)}{h_1+2h_2\left(k_{x1}^2+k_y^2\right)}\right|,\\ T_2&=\mathrm{Re}\left[\frac{k_{x4}}{k_{x1}}\right]|t_2|^2\left|\frac{h_1+2h_2\left(k_{x4}^2+k_y^2\right)}{h_1+2h_2\left(k_{x1}^2+k_y^2\right)}\right|,\end{aligned} \tag{8}$$

respectively.

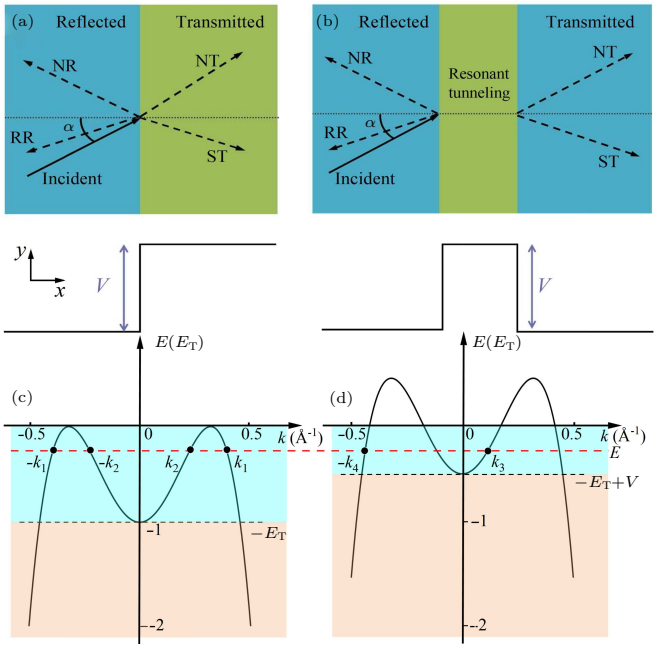


Fig. 1. Schematic illustration of the scattering processes of the Mexican-hat-dispersion electrons at the interfaces of a step (a) and rectangular (b) potential barrier. The solid and the dashed arrows denote the group velocities of the incident and the outgoing electrons, respectively. The height of the potential barrier is V and the barrier width in panel (b) is L. Energy bands of the scattering regions without (c) and with (d) potential barrier.

Similarly, if the electron is incident with another wave vector k_2, as indicated in Fig. 1(c). For electron energies within the Mexican-hat regime. In this case, the wave functions in the two regions can be expressed respectively as

$$\begin{aligned}\psi_1&=\mathrm{e}^{\mathrm{i}k_{x2}x}+\widetilde{r}_1\mathrm{e}^{-\mathrm{i}k_{x2}x}+\widetilde{r}_2\mathrm{e}^{\mathrm{i}k_{x1}x},\\ \psi_2&=\widetilde{t}_1\mathrm{e}^{\mathrm{i}k_{x3}x}+\widetilde{t}_2\mathrm{e}^{-\mathrm{i}k_{x4}x}.\end{aligned} \tag{9}$$

After a similar calculation procedure, the reflection and the transmission coefficients $\widetilde{r}_1, \widetilde{r}_2, \widetilde{t}_1, \widetilde{t}_2$ are obtained as

$$\begin{aligned}\widetilde{r}_1&=\frac{-(k_{x1}-k_{x2})(k_{x2}-k_{x3})(k_{x2}+k_{x4})}{(k_{x2}-k_{x4})(k_{x1}+k_{x2})(k_{x2}+k_{x3})},\\ \widetilde{r}_2&=-2k_{x2}\frac{(k_{x2}-k_{x3})(k_{x2}+k_{x4})}{(k_{x1}-k_{x3})(k_{x1}+k_{x2})(k_{x1}+k_{x4})},\\ \widetilde{t}_1&=2k_{x2}\frac{(k_{x1}-k_{x2})(k_{x2}+k_{x4})}{(k_{x1}-k_{x3})(k_{x2}+k_{x3})(k_{x3}+k_{x4})},\\ \widetilde{t}_2&=-2k_{x2}\frac{(k_{x1}-k_{x2})(k_{x2}-k_{x3})}{(k_{x2}-k_{x4})(k_{x1}+k_{x4})(k_{x3}+k_{x4})}.\end{aligned} \tag{10}$$

The corresponding probabilities for the NR, RR, ST, and NT are

$$\begin{aligned}R_1&=|\widetilde{r}_1|^2,\\ R_2&=\mathrm{Re}\left[\frac{k_{x1}}{k_{x2}}\right]|\widetilde{r}_2|^2\left|\frac{h_1+2h_2\left(k_{x1}^2+k_y^2\right)}{h_1+2h_2\left(k_{x2}^2+k_y^2\right)}\right|,\\ T_1&=\mathrm{Re}\left[\frac{k_{x4}}{k_{x2}}\right]|\widetilde{t}_2|^2\left|\frac{h_1+2h_2\left(k_{x4}^2+k_y^2\right)}{h_1+2h_2\left(k_{x2}^2+k_y^2\right)}\right|,\\ T_2&=\mathrm{Re}\left[\frac{k_{x3}}{k_{x2}}\right]|\widetilde{t}_1|^2\left|\frac{h_1+2h_2\left(k_{x3}^2+k_y^2\right)}{h_1+2h_2\left(k_{x2}^2+k_y^2\right)}\right|,\end{aligned} \tag{11}$$

respectively.

According to the transmission probabilities obtained above, the total conductance of the junction at zero temperature is

$$G=\sum_s 2G_0\int_{-\pi/2}^{\pi/2}(T_1^s+T_2^s)\cos\alpha\,\mathrm{d}\alpha, \tag{12}$$

where $s=-k_{x1}, k_{x2}$ denotes different incident wave vectors, $\alpha=\arctan(k_y/k_x)$ is the incident angle, and $G_0=\frac{e^2}{h}N_0(E)$. Here $N_0(E)=\frac{W|k_s|}{\pi}$ is the transverse modes in a sheet of Mexican hat dispersion materials with width W.

For electron energy outside the Mexican-hat regime, $E<-E_\mathrm{T}$, as indicated by the light yellow region in Fig. 1(c), the scattering process returns to the normal case. There is only one incident, transmission and reflection state, respectively and the wave functions in the two regions are reduced to

$$\psi_1=\mathrm{e}^{-\mathrm{i}k_{x1}x}+r_1\mathrm{e}^{\mathrm{i}k_{x1}x},\quad \psi_2=t_2\mathrm{e}^{-\mathrm{i}k_{x4}x}. \tag{13}$$

Considering the continuity of the wave function at the interface $1+r_1=t_2$, and the conservation of the probability current requires that

$$-k_{x1}\left(h_1+2h_2\left(k_{x1}^2+k_y^2\right)\right)+k_{x1}\left(h_1+2h_2\left(k_{x1}^2+k_y^2\right)\right)R_1$$

$$= -k_{x4}\left(h_1+2h_2\left(k_{x4}^2+k_y^2\right)\right)T_2, \tag{14}$$

we obtain

$$r_1 = \frac{k_{x1}\left(h_1+2h_2\left(k_{x1}^2+k_y^2\right)\right)-k_{x4}\left(h_1+2h_2\left(k_{x4}^2+k_y^2\right)\right)}{k_{x4}\left(h_1+2h_2\left(k_{x4}^2+k_y^2\right)\right)+k_{x1}\left(h_1+2h_2\left(k_{x1}^2+k_y^2\right)\right)}, \tag{15}$$

$$t_2 = \frac{2k_{x4}\left(h_1+2h_2\left(k_{x4}^2+k_y^2\right)\right)}{k_{x4}\left(h_1+2h_2\left(k_{x4}^2+k_y^2\right)\right)+k_{x1}\left(h_1+2h_2\left(k_{x1}^2+k_y^2\right)\right)}, \tag{16}$$

$$R_1 = |r_1|^2, \quad T_2 = \mathrm{Re}\left[\frac{k_{x4}}{k_{x1}}\right]\left|\frac{h_1+2h_2\left(k_{x4}^2+k_y^2\right)}{h_1+2h_2\left(k_{x1}^2+k_y^2\right)}\right||t_2|^2. \tag{17}$$

Secondly, we consider the scattering at the interfaces of a rectangular potential barrier $V(x) = V[\Theta(x)-\Theta(x-L)]$, as shown in Fig. 1(b), where $\Theta(x)$ is a step function. In this case, the whole space is separated into three regions, i.e. the incident/reflection ($x<0$), the resonant tunneling ($0<x<L$), and the transmission ($x>L$) regions. For the injected electron with energy E and wave vector k_{x2}, the wave functions in the three regions are given as

$$\begin{aligned}
\psi_1 &= \mathrm{e}^{\mathrm{i}k_{x2}x} + r_1\,\mathrm{e}^{-\mathrm{i}k_{x2}x} + r_2\,\mathrm{e}^{\mathrm{i}k_{x1}x},\\
\psi_2 &= A_1\,\mathrm{e}^{\mathrm{i}k_{x3}x} + B_1\,\mathrm{e}^{-\mathrm{i}k_{x4}x} + A_2\,\mathrm{e}^{\mathrm{i}k_{x4}x} + B_2\,\mathrm{e}^{-\mathrm{i}k_{x3}x},\\
\psi_3 &= t_1\,\mathrm{e}^{\mathrm{i}k_{x2}x} + t_2\,\mathrm{e}^{-\mathrm{i}k_{x1}x}.
\end{aligned} \tag{18}$$

The reflection and transmission coefficients r_1, r_2, t_1, t_2 and the transmission probabilities R_1, R_2, T_1, T_2 can also be obtained by using the similar calculations in above subsection. However, complex algebraic operations are required to obtain the analytical forms of the reflection and transmission probabilities. Further, the analytical results are also complex and tedious. Therefore, the detail analytical calculation procedure and its results are not presented for conciseness while the numerical results are given in the following section.

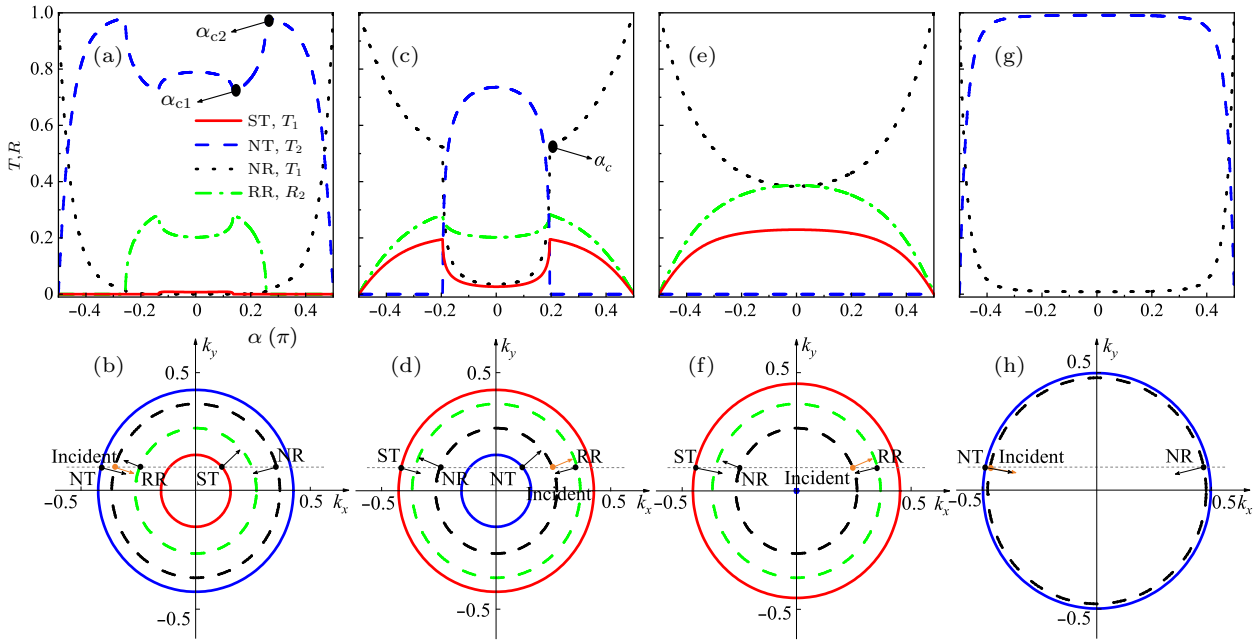


Fig. 2. Reflection and the transmission spectra as a function of the incident angle α for the scattering induced by a step potential barrier. The incident energy, barrier height, and incident wave vector k_i are set as (a) $E=-0.1$, $V=0.5$, $k_i=-k_1$; (c) $E=-0.1$, $V=0.5$, $k_i=k_2$; (e) $E=-0.1$, $V=0.9$, $k_i=k_2$; and (g) $E=-1.5$, $V=0.5$, $k_i=-k_1$. The corresponding iso-energy circles for the incident and transmitted regions are plotted in panels (b), (d), (f), and (h), respectively.

3. Numerical results and discussion

In what follows we show some numerical examples for the electron scattering and transport properties of electrons with Mexican-hat dispersion. Although, the physics discussed here do not depend on the band parameters of the Mexican-hat-dispersion, to provide specificity, the parameters of the energy band in monolayer InSe are chosen as an illustrative example, namely $h_1 = 1.478$ eV·Å^2, $h_2 = -7.219$ eV·Å^4, and $E_\mathrm{T} = 75.7$ meV.[39] The incident energy of the electron E and the hight of the electric potential V are in unit of E_T, and the barrier width of the rectangular potential is in unit of nm.

In Fig. 2(a), the reflection and transmission probabilities are plotted as a function of the incident angle at the interface of a step potential barrier. The electrons are incident with wave vector $-k_1$. The barrier height and incident energy are set as $V=0.5$ and $E=-0.1$, respectively. The corresponding iso-energy lines for the incident and transmitted regions are presented in Fig. 2(b). The radii of these concentric circles from the innermost to the outermost are $k_3 = [(-h_1+\chi)/2h_2]^{1/2}$, $k_2 = [(-h_1+\gamma)/2h_2]^{1/2}$, $k_1 = [(-h_1-\gamma)/2h_2]^{1/2}$, and $k_4 = [(-h_1-\chi)/2h_2]^{1/2}$. Given that both the reflection and transmission probabilities are even functions concerning the incident angle α, our discussions focus on the results for $\alpha>0$. When α is small, as indicated by the horizontal dashed line in Fig. 2(b), double reflections and double transmissions can be generated because the four states are all propagating modes.

Among the four propagating modes indicated in Fig. 2(b), the incident state lies between the NT state and the RR state, which indicates that the incident state is easier scattering into them as expressed in Eqs. (3)–(6). Hence, the probabilities of NT (T_2) and RR (R_2) are much larger than those of ST (T_1) and NR (R_1). Owing to the presence of ST, T_2 fails to achieve its maximum value at normal incidence, which is different from the potential scattering in conventional semiconductors.[36] T_1 increases with the escalating α, whereas, T_2 exhibits a gradual decreases as α increases until it reaches the first critical angle $\alpha_{c1} = \arcsin(k_3/k_1) = 0.14\pi$ where the horizontal dashed line becomes tangent to the red solid circle in Fig. 2(b). For $\alpha > \alpha_{c1}$, the ST state becomes evanescent wave, then T_1 vanishes. However, T_2 increases to a peak (~ 1.0) as α increases until it reaches the second critical angle $\alpha_{c2} = \arcsin(k_2/k_1) = 0.26\pi$ where the horizontal dashed line becomes tangent to the green dashed circle in Fig. 2(b). Finally, T_2 rapidly diminishes to zero as α approaches $\pi/2$. Meanwhile, R_2 displays opposite trends compared to T_2 with an increasing α up to α_{c2}, shown by the green dash–dotted line in Fig. 2(a). For $\alpha > \alpha_{c2}$, the RR state becomes evanescent wave, and R_2 vanishes, leading to a sharply increased R_1.

Figures 2(c) and 2(e) display the reflection and the transmission as a function of the incident angle α, in which electrons are incident with wave vector k_2. The incident energies are $E = -0.1$, and the barrier hight V are 0.5 and 0.9 for Figs. 2(c) and 2(e), respectively. The corresponding iso-energy lines for the incident and transmitted regions are presented in Figs. 2(d) and 2(f). The radii of these concentric are also in the order of k_3, k_2, k_1, and k_4. For small barrier $V = 0.5$, there are also four propagating states for small α as indicated by the horizontal dashed line in Fig. 2(d). Consequently, double reflections and double transmissions also appear. Among the four propagating modes, the incident state lies between the NT state and the RR state, which means that the incident state is easier scattering into them as expressed in Eq. (10). Therefore, T_2 and R_2 are much larger than T_1 and R_1. Different from the results in Fig. 2(a), T_2 reaches its maximum value at normal incidence and then decreases to zero when α increases to the critical angle $\alpha_c = \arcsin(k_3/k_2) = 0.195\pi$ where the horizontal dashed line becomes tangent to the red solid circle in Fig. 2(d). For $\alpha > \alpha_c$, T_2 vanishes because the NT state becomes evanescent wave. Whereas, T_1 increases with escalating α and achieve its maximum at α_c, then it gradually diminishes to zero as α approaches $\pi/2$. Meanwhile, R_1 displays opposite trends compared to T_2, and R_2 shows the same trends compared to T_1 with the increasing of α. For large barrier $V \geq E_T + E$, such as $V = 0.9$, the iso-energy circle corresponding to NT reduces to a point or disappears, and the ST state becomes evanescent wave. Hence, there are double reflections but only specular transmission in this case. Owing to the disappear of T_1, T_2 is greatly enhanced compared with the results in Figs. 2(a) and 2(c). For electrons with incident energy satisfying $E < -E_T$, there are only two modes of propagation, one incident state and one reflected state. The scattering caused by the step barrier is similar to that in conventional semiconductors. Figure 2(g) plots the reflection and transmission spectra as a function of α with $E = -1.5$ and barrier hight $V = 0.5$. In this case, there are only SR (R_1) and NT (T_2), as shown by the black solid and the blue dotted lines, respectively. The T_2 decreases slowly first and then drop fast with the increase of the α, whereas, R_1 demonstrates a reversal behaviour, which is similar to the results in conventional semiconductors.[36] The reason is that only the NT and SR states are propagating modes within the whole incident angle range, as shown by the iso-energy lines in Fig. 2(g).

Next, let us turn to the scattering induced by a rectangle potential barrier. Figures 3(a)–3(d) show the reflection and the transmission spectra as a function of the incident angle α for the scattering induced by a rectangle potential barrier for different barrier widths. In comparison to the results of the stepped barrier, there are two notable features in the case of the rectangle barrier. One is that the probability of ST will increase because there are two forward propagating waves in the barrier region [see Eq. (18)], and both of them produce ST at the interface $x = L$. Another is that there is resonant tunnelling. We will focus on these two features in the following discussions.

For electrons incident with wavevector $-k_1$, as shown in Figs. 3(a) and 3(c), there is a critical angle $\alpha_c = \arcsin(k_3/k_1)$ where the horizontal dashed line becomes tangent to the red solid circle in Fig. 3(e) in the reflection and transmission spectra. There are double reflections and transmissions for $0 < \alpha < \alpha_c$ with enhanced T_1 and reduced R_2 because both the two forward propagating waves produce ST at the interface $x = L$. However, T_1 and R_2 disappear for $\alpha > \alpha_c$, and T_2 (R_1) shows some resonate peaks (dips), i.e., $T_2 = 1$ ($R_1 = 0$), as the increasing of α arising from the resonate tunnelling. The resonate condition can be obtained numerically and need to be discussed in two cases because it sensitively depends on α. For $0 < \alpha < \alpha_c$, the wavevectors k_{x3} and k_{x4} both are real. We have numerical checked the resonate condition and found it requires either $e^{ik_{x3}L} = 1$ and $e^{ik_{x4}L} = 1$ or $e^{ik_{x3}L} = -1$ and $e^{ik_{x4}L} = -1$. Therefore, we have $k_{x3}L = m\pi$ and $k_{x4}L = n\pi$, where m and n are both odd or even. The resonate condition indicates large barrier width L is needed to generate resonate tunnelling for $0 < \alpha < \alpha_c$. Hence, we only observe resonate tunneling within this angle region for $L = 50$ in Fig. 3(c). For $\alpha > \alpha_c$, the wavevector k_{x3} becomes imaginary while k_{x4} is still real. By numerical calculation, we find the resonate condition becomes $e^{ik_{x4}L} = \pm 1$, i.e., $k_{x4}L = n\pi$ where n is a nonzero integer, which is similar to that in conven-

tional semiconductors.[36] The condition $k_{x4}L = n\pi$ means that the wider the potential barrier, the more the resonate peaks, which can be directly observed in Fig. 3(c) as indicated by the blue dashed line. For electrons incident with wavevector k_2, as shown in Figs. 3(b) and 3(d), T_1 is greatly enhanced in comparison to the results induced by a stepped barrier. For a short barrier such as $L = 10$ nm, T_1 and R_2 does not decrease to zero immediately when α exceeds the critical angle α_c [see Fig. 3(b)]. Although the states k_{x3} becomes evanescent wave, it can still penetrate a short barrier. For a wider barrier such as $L = 50$ nm, T_1 only shows some resonate peaks for $0 < \alpha < \alpha_c$. The resonate condition is also $k_{x3}L = m\pi$ and $k_{x4}L = n\pi$, where m and n are both odd or even.

In order to understand the quantum transport properties of the junctions shown in Figs. 1(a) and 1(b), the ballistic conductances as a function of incident energy for the step and rectangle barriers are plotted in Figs. 4(a)–4(d) with various potentials such as $V = 0$, 0.1, 0.5, and 0.9, where G_1 (G_2) denotes the conductance of electrons incident with $-k_1$ (k_2), and G_T stands for the total conductance. As shown in Fig. 4(a), the conductance G_1 tends toward saturation with the decreasing incident energy for all barrier cases. The saturation conductance of G_1 diminishes as the barrier potential V increases. This decrease in saturation conductance is attributed to the barrier obstructing the normal and specular transmissions, thereby causing an overall reduction in transmission. Concurrently, G_1 undergoes mutation at incident energy $E = -E_T$ since the density of state in the incident region undergoes an abrupt transition. Moreover, the magnitude of these mutations becomes more pronounced with larger values of V, which is attributed to the suppression of the normal transmission. Conversely, as plotted in Fig. 4(b), G_2 initially experiences an ascent followed by a descent as the decreasing of the incident energy for all barrier cases. It increases first with the decrease of the incident energy and reaches its maximum around $E = (V - E_T)/2$. However, it diminishes nonlinearly as the incident energy is decreased to $E = (V - E_T)$. After that, the conductance diminishes linearly as the incident energy is decreased further to $E = -E_T$. This phenomenon can be elucidated by the fact that, when E is below $V - E_T$, the k_{x3} state in the transmission region becomes an evanescent wave, leading to a sharp decrease in the normal transmission T_2 as shown by the blue-dashed line in Fig. 3(e). Moreover, when E is less than the brim of the Mexican-hat dispersion E_T, namely $E < -E_T$, the incident k_2 state becomes an evanescent wave, preventing transmission and resulting G_2 going straight to zero.

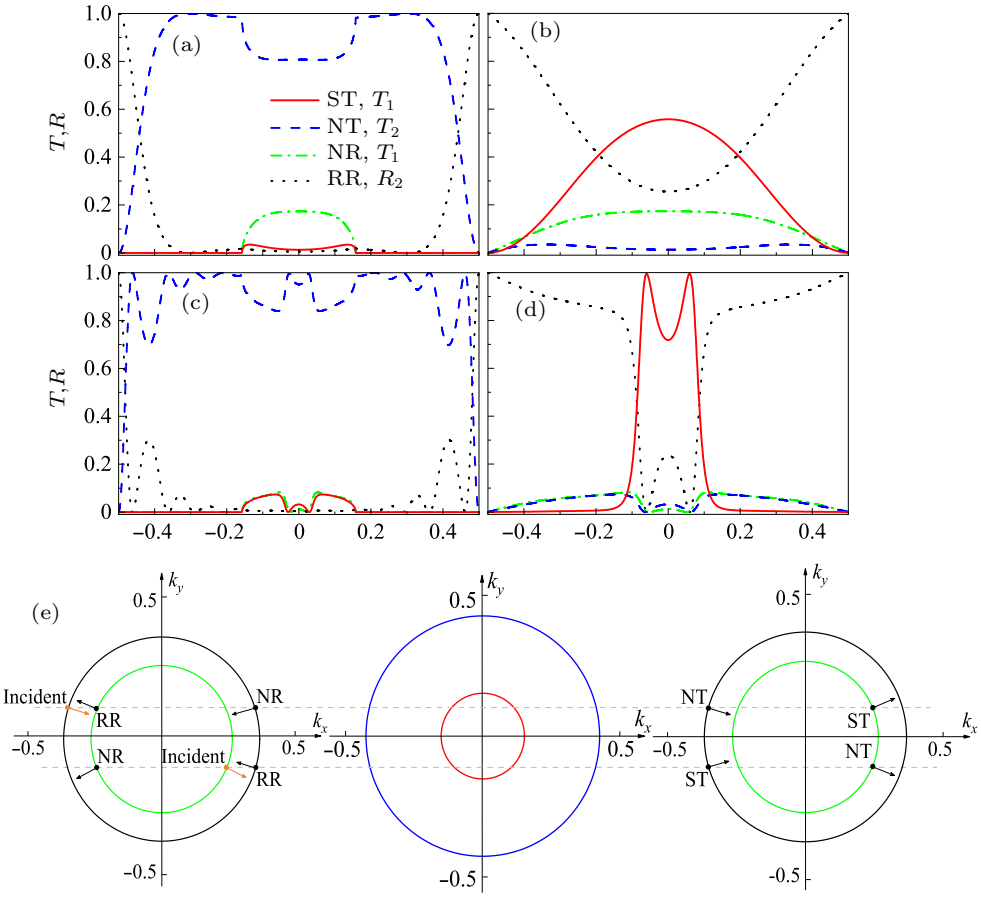


Fig. 3. (a)–(d) Reflection and the transmission spectra as a function of the incident angle α for the scattering induced by a rectangle potential barrier. The incident energy and the barrier height are -0.4 and 0.5, respectively. The barrier width, and incident wave vector k_i are set as (a) $L = 10$ nm, $k_i = -k_1$; (b) $L = 10$ nm, $k_i = k_2$; (c) $L = 50$ nm, $k_i = -k_1$; and (d) $L = 50$ nm, $k_i = k_2$. The corresponding iso-energy circles for the incident, center, and transmitted regions are plotted in panel (e).

Now, let us turn back to the total conductance G_T depicted in Fig. 4(c) which is measured experimentally. As discussed in Figs. 4(a) and 4(b), G_1 tends to saturate with decreasing incident energy, while G_2 ascends first and then descends gradually. Consequently, the behavior of the total conductance $G_T = G_1 + G_2$ versus the incident energy shows a combination effect from those of G_1 and G_2. The total conductance also exhibits an ascent followed by a descent with decreasing incident energy for all barrier cases within the energy range of $(V - E_T) < E < 0$. Otherwise, it maintains a saturation value. In addition, the total conductance mutations are also observed at $E = -E_T$ for all potential barriers, which can be used to determine the height of the Mexican-hat dispersion. When the potential V is absent, ideal quantized conductance plateaus are observed (see the black dashed line). The step feature in the conductance spectrum reflects the van Hove singularity in the DOS spectrum,[24–32] which is an indirect evidence for the Mexican-hat band structure. However, the conductance plateau within the energy range $-E_T < E < 0$ is destroyed as the potential barrier is presented and the maximum value of the conductance decreases with increasing V. When the electrical potential V exceeds E_T, the variation of the total conductance vanishes because there is only normal reflection and transmission in this case. Therefore, it is evident that the total conductance can be effectively controlled by adjusting the barrier potential V. For the total conductance of the system with a rectangle barrier, as shown in Fig. 4(d), its characteristics are similar to those in Fig. 4(c).

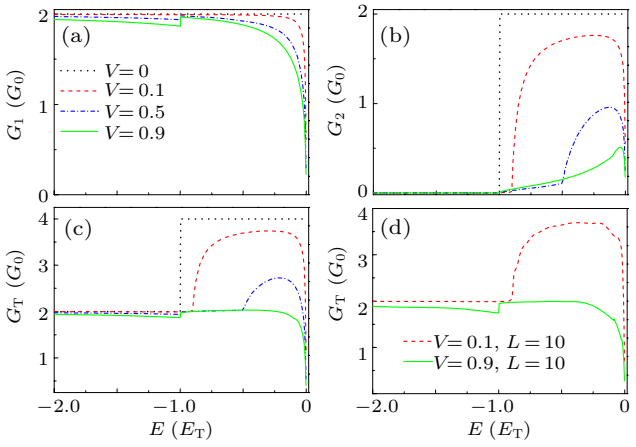


Fig. 4. (a)–(c) The ballistic conductance as a function of incident energy for a step barrier with various potentials. (a) G_1 stands for electrons incident with wavevector $-k_1$. (b) G_2 denotes electrons incident with wavevector k_2. (c) $G_T = G_1 + G_2$ is the total conductance. (d) The total conductance as a function of incident energy for a rectangle barrier with various potentials.

Figure 5 presents the conductances as a function of the barrier width for $E = -0.4$ under various potentials. As shown in Fig. 5, the conductances can be examined in two distinct scenarios. In the regime where $V < E + E_T$, both k_{x3} and k_{x4} are real and there are four propagation modes within the barrier region, i.e., two forward and two backward. The oscillations of both G_1 and G_2 with respect to barrier width L reveal a nuanced dynamic, characterized by the smaller oscillation period of G_1 compared to that of G_2 as indicated by the red and blue lines in Figs. 5(a) and 5(b). A discernible phase difference further distinguishes these oscillations. As the increasing of the barrier potential V, the amplification of this period difference becomes evident, ushering in the emergence of multiple periods in the conductance G_T. This phenomenon is particularly pronounced at elevated barrier potentials as shown in the red and blue lines in Fig. 5(c). As discussed in Fig. 4, the k_{x3} states matches the incident state k_2 better compared with the state k_{x4}. However, under the condition $V > E + E_T$, the wavevector k_{x3} becomes imaginary while k_{x4} remains real. Consequently, G_1 persists in its oscillations with L, while G_2 undergoes a substantial diminishment and cessation of oscillation as denoted by the green lines in Figs. 5(a) and 5(b). Consequently, in this distinctive scenario, the conductance G_T is unequivocally dominated by the oscillatory behavior of G_1 as indicated by the green lines in Fig. 5(c).

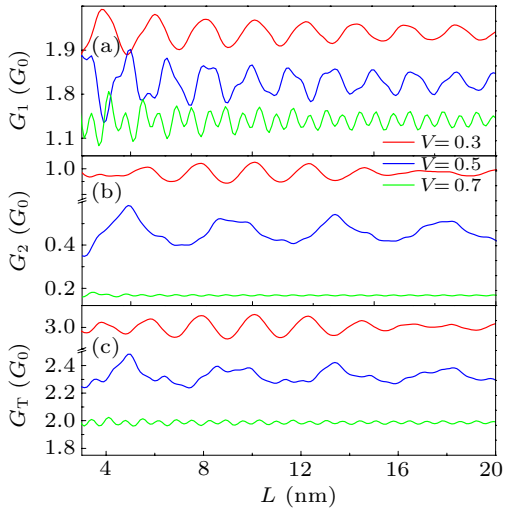


Fig. 5. Conductances as a function of the barrier width for $E = -0.4$ under various potentials, where (a) for G_1, (b) for G_2, and (c) for G_T.

4. Summary

In summary, we studied the quantum scattering and transport of electrons with Mexican-hat dispersion through both step and rectangular potential barriers by using the transfer matrix method. For the step potential with electrons incident from the large wavevector, the transmission is primarily governed by NT with nearly negligible ST, while the reflection is dominant by RR (NR) within (outside) the critical angle. Additionally, for electrons incident from the small wavevector, the NT can be reduced to zero by adjusting the barrier, resulting in a significant enhancement of ST and RR. For the rectangular barrier, the transmission and reflection spectra resemble those of the step barrier, but there are two kinds of resonant tunneling which can lead to perfect NT or ST. As a result of the abnormal scattering process, the conductance of the system can be effectively controlled by adjusting the height

and width of the barrier as well as the incident energy. Moreover, the height of the Mexican-hat dispersion can also be detected from the conductance behaviours. Our results may benefit to further understand the electron states governed by the Mexican-hat dispersion.

Acknowledgements

Project supported by the National Natural Science Foundation of China (Grant Nos. 12374071, 12174100, 12164021, and 11804092) and the Natural Science Foundation of Jiangxi Province, China (Grant No. 20212ACB201005).

References

[1] Novoselov K S, Geim A K, Morozov S V, Jiang D, Zhang Y, Dubonos S V, Grigorieva I V and Firsov A A 2004 *Science* **306** 666
[2] Sahin H, Cahangirov S, Topsakal M, Bekaroglu E, Akturk E, Senger R T and Ciraci S 2009 *Phys. Rev. B* **80** 155453
[3] Yu S, Wu X, Wang Y, Guo X and Tong L 2017 *Adv. Mater.* **29** 1606128
[4] Gibertini M, Koperski M, Morpurgo A F and Novoselov K S 2019 *Nat. Nanotechnol.* **14** 408
[5] Gao G, Ding G, Li J, Yao K, Wu M and Qian M 2016 *Nanoscale* **8** 8986
[6] Cai H, Gu Y, Lin Y C, Yu Y, Geohegan D B and Xiao K 2019 *Appl. Phys. Rev.* **6** 041312
[7] Vu T V, Phuc H V, Nhan L C, Kartamyshev A I and Hieu N N 2023 *J. Phys. D: Appl. Phys.* **56** 135302
[8] Novoselov K S, Geim A K, Morozov S V, Jiang D, Katsnelson M I, Grigorieva I V, Dubonos S V and Firsov A A 2005 *Nature* **438** 197
[9] Mak K F, Lee C, Hone J, Shan J and Heinz T F 2010 *Phys. Rev. Lett.* **105** 136805
[10] Zólyomi V, Drummond N D and Fal'ko V I 2013 *Phys. Rev. B* **87** 195403
[11] Min H, Sahu B, Banerjee S K and MacDonald A H 2007 *Phys. Rev. B* **75** 155115
[12] Jiang Y, Thapa S, Sanders G D, Stanton C J, Zhang Q, Kono J, Lou W K, Chang K, Hawkins S D, Klem J F, Pan W, Smirnov D and Jiang Z 2017 *Phys. Rev. B* **95** 045116
[13] Magorrian S J, Zólyomi V and Fal'ko V I 2016 *Phys. Rev. B* **94** 245431
[14] Jappor H R and Habeeb M A 2018 *Current Appl. Phys.* **18** 673
[15] Ariapour M and Babaee S T 2020 *J. Magn. Magn. Mater.* **510** 166922
[16] Bandurin D A, Tyurnina A V, Yu G L, Mishchenko A, Zólyomi V, Morozov S V, Krishna Kumar R, Gorbachev R V, Kudrynskyi Z R, Pezzini S, Kovalyuk Z D, Zeitler U, Novoselov K S, Patanè A, Eaves L, Grigorieva I V, Fal'ko V I, Geim A K and Cao Y 2017 *Nat. Nanotechnol.* **12** 223
[17] Demirci S, Avazlı N, Durgun E and Cahangirov S 2017 *Phys. Rev. B* **95** 115409
[18] Kibirev I A, Matetskiy A V, Zotov A V and Saranin A A 2018 *Appl. Phys. Lett.* **112** 191602
[19] Hu T, Zhou J and Dong J 2017 *Phys. Chem. Chem. Phys.* **19** 21722
[20] Zhou M, Zhang R, Sun J, Lou W K, Zhang D, Yang W and Chang K 2017 *Phys. Rev. B* **96** 155430
[21] Skinner B 2016 *Phys. Rev. B* **93** 235110
[22] Xiao X B, Ye Q, Liu Z F, Wu Q P, Li Y and Ai G P 2019 *Nanoscale Res. Lett.* **14** 322
[23] Ye Q, Tang S X, Du Y, Liu Z F, Wu Q P and Xiao X B 2024 *J. Phys.: Condens. Matter* **36** 365501
[24] Nurhuda M, Nugraha A R T, Hanna M Y, Suprayoga E and Hasde E H 2020 *Adv. Nat. Sci: Nanosci. Nanotechnol.* **11** 015012
[25] Seixas L, Rodin A S, Carvalho A and Neto A H C 2016 *Phys. Rev. Lett.* **116** 206803
[26] Ghobadi N and Rezavand A 2022 *Mater. Sci. Semicond. Process.* **152** 107061
[27] Cao T, Li Z and Louie S G 2015 *Phys. Rev. Lett.* **114** 236602
[28] Wickramaratne D, Zahid F and Lake R K 2015 *J. Appl. Phys.* **118** 075101
[29] Ge X J, Qin D, Yao K L and Lü J T 2017 *J. Phys. D: Appl. Phys.* **50** 405301
[30] Houssa M, Meng R, Iordanidou K, Pourtoi G, Afanas'ev V V and Stesmans A 2021 *J. Comput. Electron.* **20** 88
[31] Heremans J P, Jovovic V, Toberer E S, Saramat A, Kurosaki K, Charoenphakdee A, Yamanaka S and Snyder G J 2008 *Science* **321** 554
[32] Zólyomi V, Drummond N D and Fal'ko V I 2014 *Phys. Rev. B* **89** 205416
[33] Zhou M, Zhang D, Yu S, Huang Z, Chen Y, Yang W and Chang K 2019 *Phys. Rev. B* **99** 155402
[34] Zhou M, Yu S, Yang W, Lou W K, Cheng F, Zhang D and Chang K 2019 *Phys. Rev. B* **100** 245409
[35] Li Y Q, Chen X R, Luo W, Zhou T and Chen W 2022 *Europhys. Lett.* **137** 36003
[36] Griffiths D J 2016 *Introduction to Quantum Mechanics* (Cambridge University Press)
[37] Cheianov V V, Fal'ko V I and Altshuler B L 2007 *Science* **315** 1252
[38] Lee G H, Park G H and Lee H J 2015 *Nat. Phys.* **11** 925
[39] Zhou M 2021 *Phys. Rev. B* **103** 155429
[40] Ruhl J 2015 *Quantum Mechanics with a Quartic Dispersion Law*, Graduate Masters Theses 339